# Turbulence- and buoyancy-driven secondary flow in a horizontal square duct heated from below

A. Sekimoto, G. Kawahara, and K. Sekiyama

*Department of Mechanical Science, Osaka University, 560-8531 Osaka, Japan* *

M. Uhlmann

*Institute for Hydromechanics, Karlsruhe Institute of Technology, 76128 Karlsruhe, Germany*

A. Pinelli

*Modeling and Numerical Simulation Unit, CIEMAT, 28040, Madrid, Spain*

(Dated: May 30, 2010)

## Abstract

Direct numerical simulations of fully developed low Reynolds number turbulent flows in a horizontal square duct heated from below are performed at bulk Reynolds numbers $Re_b = 3000$ and 4400 (based on duct width, $H$) and bulk Richardson numbers $0 \leq Ri \leq 1.03$. The primary objective of the numerical simulations concerns the characterization of the mean secondary flow that develops in this class of flows. On one hand, it is known that turbulent isothermal flow in a square duct presents secondary mean motions of Prandtl's second kind that find their origin in the turbulent coherent structures behavior. On the other hand, thermal convection effects induce a mean secondary motion of Prandtl's first kind directly induced by buoyancy. The first analysis that will be presented concerns the determination of the correct scaling laws for the integral quantities that characterize the mean thermo-fluid behavior. In particular, the mean cross motion and its r. m. s. fluctuations are found to scale with the buoyancy induced velocity $u_g$ and with the product of the latter with the magnitude of the viscous velocity (i.e., $\sqrt{(\nu/H)u_g}$, being $H$ the duct width and $\nu$ the kinematic viscosity), respectively. The correct scalings for the r. m. s. of streamwise velocity component and of temperature fluctuations are found to be related also with the friction velocity $u_\tau$ and friction temperature $T_\tau$ according to the magnitudes $u_\tau^2/\sqrt{(\nu/H)u_g}$ and $T_\tau u_\tau/\sqrt{(\nu/H)u_g}$, respectively. As far as the mean structure of the cross motion is concerned, it is found that different types of secondary flow regimes take place when increasing the value of Richardson number. In particular, the mean secondary flow found in the range $0.025 \lesssim Ri \lesssim 0.25$ is characterized by a single large-scale thermal convection roll and four turbulence-driven corner vortices as opposed to the classical scenario of the eight-vortex secondary flow pattern typical of isothermal turbulent flows. When increasing the value of Richardson number (i.e., $Ri \gtrsim 0.25$) the structure of the mean secondary flow is solely determined by the large-scale circulation induced by the buoyancy force. In this regime, the mean cross motion is characterized by the presence of two counter-clockwise rotating vortices located near the upper-left and lower-right corners. As expected, it is found that the secondary flow regime strongly affects the magnitude and the local behaviour of integral quantities like the skin friction coefficient and the heat transfer rate.



PACS numbers: Valid PACS appear here



*Electronic address: kawahara@me.es.osaka-u.ac.jp

## I. INTRODUCTION

The existence of secondary flow of Prandtl's second kind is a well-known phenomenon in fully developed turbulent square duct flow [1]. Although relatively weak, secondary flow plays an important role in the cross-streamwise transport of heat, mass and momentum. A complete understanding of the intimate generation mechanisms leading to the appearance of the mean secondary flow would pave the way for introducing technological improvements in real world applications and for enhancing the capabilities of turbulence models to predict turbulent mean motions of Prandtl's second kind. In the past, there have been many studies focusing on the budget of the Reynolds stress tensor and their eventual anisotropy [3, 4] with the objective to explain the generation of this mean motion. Those studies were mainly focused upon the budget of the averaged flow equations, while not providing much information on the underlying physical mechanisms responsible for the formation of secondary flow. [The preceeding sentence has already been repeated too many times by us!]

Detailed investigations of the role of the dynamics of coherent structures in low Reynolds number isothermal turbulent duct flow has been recently carried out by the present authors [5, 12]. The mentioned work has highlighted the important role played by the sidewalls which constrain the spanwise statistical distribution of coherent structures near the wall, i.e. quasi-streamwise vortices, low- and high-speed streaks. It has been shown that the resulting preferential locations of those structures is intimately related to the pattern of the secondary flow in the isothermal cases.

In thermal square-duct turbulence under the action of gravity, which we shall discuss in this paper, the mean secondary flow will be driven not only by turbulence but also by buoyancy, and thus their combined effects should be taken into consideration for characterization of the secondary motion. The behavior of near-wall turbulence structures in square-duct flow with heated walls was previously addressed by Salinas Vázquez *et. al.* [6] using large eddy simulations of compressible flow at low Mach number. They have shown that the size limitation imposed by the lateral walls leads to a single low-speed streak located near the duct central plane surrounded by two high-speed streaks on both sides. The ejection motion near the heated wall is enhanced by heating, which contributes to the breaking of the symmetries of the usual secondary flow of the second kind. These authors have not considered the case with strong buoyancy effects, in which a large-scale thermal convection

roll appears, leading to a strong enhancement on the heat transfer rate. The buoyancy effects on statistics of square-duct turbulence have been studied by Ma *et. al.* [7] by carrying out Direct Numerical Simulations (DNS), with temperature difference imposed between the vertical walls, considering a wide range of Grashof numbers. They have shown that at higher Grashof numbers, a large scale circulation motion (we shall call it secondary flow of Prandtl's first kind) induced by buoyancy force has a strong impact on the budget of energy also producing a strong enhancement of heat flux on the hot wall. Ma *et. al.* [7] also report that, when increasing the Grashof number, the mean secondary flow of Prandtl's second kind may experience a change to a four-vortex pattern by virtue of the thermal convection induced by the buoyancy force. In particular they have shown the existence of a single large-scale circulation roll surrounded by smaller-corner secondary flow vortices with opposite sign of rotation. However, the authors did not propose any physical mechanism responsible for the formation of such a peculiar four-vortex pattern secondary flow and its eventual relationship with near-wall turbulent coherent structures and their modifications in the presence of buoyancy effects. In the present contribution we extend the findings of isothermal square-duct turbulence in references [5, 12] to the case of a non-isothermal configuration. Through high fidelity numerical simulations we determine the role played by the coherent vortical structures embedded in the flow field in producing the pattern of the mean turbulent flow.

In this study, we characterize the secondary flow of Prandtl's first and second kind by using the result of direct numerical simulations (DNS) of fully developed turbulent flow in a horizontal square duct heated from below at low Reynolds numbers. Firstly, we determine the functional relationship of the wall friction coefficient and of the Nusselt number from the Richardson number. Moreover, we reveal the correct scaling for the mean quantities and their fluctuations using a careful analysis of the mean equations supplemented by results obtained through DNS. Next, we show that the secondary flow patterns drastically change when increasing the bulk Richardson number which represents the ratio of buoyancy force and inertial force. On one hand, under weak buoyancy effect, we can observe the usual secondary flow of Prandtl's second kind which is characterized by an eight-vortex pattern. On the other hand, when considering stronger thermal effects, the secondary flow is predominantly driven by buoyancy force leading to a large-scale circulation roll similar to the one found in a natural convection scenario concerning a two-dimensional square container [8] with the temperature

difference imposed between horizontal walls. In-between those extreme conditions, when the intensity of the buoyancy-induced velocity is comparable with the turbulence-induced velocity one, we can observe a transitional regime whose mean secondary flow presents a mixed pattern characterized by the presence of a large scale circulation and of four small-scale vortices near the corners which sense of rotation is opposite to the large-scale circulation one. We will also address the modifications of wall structures under the direct influence of buoyancy and the buoyancy induced large recirculacion to shed some light on the nature and origin of the residual four vortex Prandtl's motions of second kind in this particular regime.

## II. NUMERICAL PROCEDURE AND VALIDATION

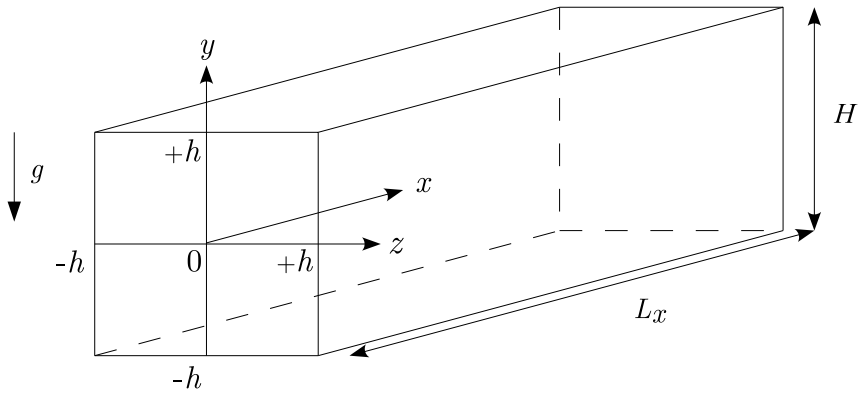


FIG. 1: Flow configuration and coordinate system.

We consider an incompressible viscous fluid flowing through an infinitely straight and horizontal square duct. As shown in Fig. 1, a Cartesian coordinates $(x, y, z)$ system is introduced such that $x$ denotes the streamwise direction and $y$-$z$ denote the cross-stream plane $[-h,\ h]\times[-h,\ h]$, $h$ being the duct half width. The vertical upward direction (i.e., gravity opposite direction) is represented by $y$, while $x$-, $z$-axes are parallel to the horizontal plane. All the simulations were performed imposing a constant mass flow rate. Also a constant temperature difference is given between top (cold) and bottom (hot) walls (i.e., unstable temperature stratification). The side walls are modeled as perfectly insulated ones.

The time evolution of the velocity vector $\boldsymbol{u} = (u, v, w)$, the pressure $p$ and the temperature $T$ will be described by means of the incompressible Navier-Stokes equations using the

Boussinesq approximation and a transport equation for the temperature (energy equation):

$$\frac{\partial \boldsymbol{u}}{\partial t} + (\boldsymbol{u}\cdot\nabla)\boldsymbol{u} = -\frac{1}{\rho}\nabla p + \nu\nabla^2\boldsymbol{u} + g\beta(T-T_0)\boldsymbol{e}_y, \tag{1}$$

$$\nabla\cdot\boldsymbol{u} = 0, \tag{2}$$

$$\frac{\partial T}{\partial t} + (\boldsymbol{u}\cdot\nabla)T = \kappa\nabla^2 T. \tag{3}$$

In (1), $\boldsymbol{e}_y$ is the unit vector associated to the $y$-direction, $\rho$ is the constant mass density, $\nu$ is the kinematic viscosity (also considered to be a constant), $g$ ($>0$) is the gravity acceleration and $T_0$ is the reference temperature: $T_0 = \frac{1}{2}(T_c + T_h)$ ($T_h$ and $T_c$ being the temperatures of the heated bottom wall and of the cooled top wall, respectively). In (3), $\beta$ is the volumetric coefficient of thermal expansion and $\kappa$ is the thermal diffusion coefficient. Equations (1) and (2) are advanced in time by means of a pressure correction method [9]. In particular, we use a semi-implicit scheme for the diffusive terms, and a three-step low-storage Runge-Kutta method with an explicit treatment for the convective and buoyant terms:

$$\frac{\boldsymbol{u}^* - \boldsymbol{u}^{k-1}}{\Delta t} = -2\alpha_k\frac{1}{\rho}\nabla p^{k-1} - \gamma_k[(\boldsymbol{u}\cdot\nabla)\boldsymbol{u} - g\beta(T-T_0)\boldsymbol{e}_y]^{k-1} - \zeta_k[(\boldsymbol{u}\cdot\nabla)\boldsymbol{u} - g\beta(T-T_0)\boldsymbol{e}_y]^{k-2} + \alpha_k\nu\nabla^2(\boldsymbol{u}^* + \boldsymbol{u}^{k-1}) \tag{4}$$

$$\nabla^2\phi^k = \frac{\nabla\cdot\boldsymbol{u}^*}{2\alpha_k\Delta t} \tag{5}$$

$$\boldsymbol{u}^k = \boldsymbol{u}^* - 2\alpha_k\Delta t\nabla\phi^k \tag{6}$$

$$p^k = p^{k-1} + \phi^k - \alpha_k\Delta t\nu\nabla^2\phi^k, \tag{7}$$

where $k = 1, 2, 3$ is the Runge-Kutta step count ($k = 3$ being equivalent to the next time step), $\boldsymbol{u}^*$ is the predicted non-solenoidal velocity vector, and $\phi$ is the pseudo pressure. A set of coefficients leading to a second-order temporal accuracy for velocity and pressure [9] is $\alpha_k = \left[\frac{4}{15},\ \frac{1}{15},\ \frac{1}{6}\right]$, $\gamma_k = \left[\frac{8}{15},\ \frac{5}{12},\ \frac{3}{4}\right]$, $\zeta_k = \left[0,\ -\frac{17}{60}, -\frac{5}{12}\right]$. In a similar fashion, the semi-discrete version of equation (3)

$$\frac{T^k - T^{k-1}}{\Delta t} = -\gamma_k[(\boldsymbol{u}\cdot\nabla)T]^{k-1} - \zeta_k[(\boldsymbol{u}\cdot\nabla)T]^{k-2} + \alpha_k\kappa\nabla^2(T^k + T^{k-1}). \tag{8}$$

guarantees a second order temporal accuracy for the temperature field as well. As far as the spatial discretization is concerned, a discrete Fourier expansion is employed to approximate the variables in the streamwise ($x$) direction, while Chebyshev polynomials are used in the cross-streamwise ($y, z$) directions. The convective terms are evaluated pseudo-spectrally with the 2/3 dealiasing technique applied only in the Fourier direction. A Fourier-Galerkin

treatment of the elliptic operators arising from the semi-discretized system gives rise to a set of Helmholtz and Poisson problems to be solved for each Fourier coefficient. These bidimensional problems are tackled in an efficient manner using a fast diagonalisation technique [10]. More details about the algorithm and its validation in isothermal configurations are given in Pinelli *et. al.* [12].

Three non-dimensional parameters that govern the flow are the bulk Reynolds number, the Prandtl number and the bulk Richardson number, defined as:

$$Re_b = \frac{u_b H}{\nu}, \quad Pr = \frac{\nu}{\kappa}, \quad Ri = \frac{g\beta\Delta T H}{{u_b}^2}, \tag{9}$$

where $H$ is full duct width ($H = 2h$), $u_b$ is the bulk mean velocity, and $\Delta T = T_h - T_c$ is the temperature difference between the upper and lower walls. The bulk Richardson number, formed by the ratio of the buoyancy force and the inertial force, can be recast in terms of the Grashof number $Gr$ ($Gr = g\beta\Delta T H^3/\nu^2$) and $Re_b$, as $Ri = GrRe_b^{-2}$. Another, alternative expression for the Richardson number is $Ri = (u_g/u_b)^2$, where $u_g = \sqrt{g\beta\Delta T H}$ is the velocity scale associated with buoyancy. Other non-dimensional groups that will be used hereafter are the friction Reynolds number $Re_\tau$ and the Nusselt number $Nu$ which are defined as follows: $Re_\tau = u_\tau h/\nu$, where $u_\tau = \sqrt{\langle\tau_w\rangle_4/\rho}$, is the friction velocity ( $\tau_w$ being the wall shear stress and $\langle\cdot\rangle_4$ the average computed over time and over the four walls). $Nu = q_w H/(\kappa\Delta T)$ will denote the local Nusselt number, where $q_w$ is the local heat flux on the horizontal walls. $\langle Nu\rangle_2$ will refer to the mean Nusselt number where $\langle\cdot\rangle_2$ is the average computed over time and over the two horizontal walls. Finally, from now on, variables with a + superscript will refer to variables normalized with $u_\tau$ and $\nu$.

In the following we present results from simulations performed at two Reynolds numbers: $Re_b = 3000$ and 4400. For each value of the Reynolds number, Richardson numbers are chosen in the range $0 \leq Ri \leq 1.03$. At large value of $Ri$, the Boussinesq approximation can still be considered as an acceptable one in cases of square ducts with a large width and an imposed small temperature difference. The Prandtl number $Pr$ is fixed to 0.71 (i.e., the working fluid is air). The values of the parameters used for each undertaken numerical simulation are summarized in Table I.

All the simulations have been carried out choosing a spatial discretization verifying the following criteria: the number of Fourier modes are determined in such a way that the streamwise grid spacing is below 16.4 wall units ($\Delta x^+ = \Delta x u_\tau/\nu < 16.4$); the number of

TABLE I: Simulation parameters

| | $Re_b$ | $Re_\tau$ | $Gr$ | $Ri$ | $\delta x^+$ | $\max\{\delta y^+, \delta z^+\}$ | $\delta t^+$ | $T_{\mathrm{stat}}\, u_b/h$ |
|---|---|---|---|---|---|---|---|---|
| (a) | 3000 | 105.4 | $5.0 \times 10^3$ | 0.00056 | 10.4 | 3.4 | 0.071 | 2651 |
| (b) | 3000 | 107.0 | $2.0 \times 10^5$ | 0.022 | 10.5 | 3.47 | 0.074 | 6555 |
| (c) | 3000 | 111.2 | $5.0 \times 10^5$ | 0.056 | 10.9 | 3.6 | 0.080 | 2651 |
| (d) | 3000 | 142.19 | $9.0 \times 10^6$ | 1.00 | 14.0 | 4.6 | 0.13 | 2603 |
| (e) | 4400 | 149.3 | $5.0 \times 10^3$ | 0.00026 | 14.7 | 4.83 | 0.097 | 2333 |
| (f) | 4400 | 150.6 | $4.3 \times 10^5$ | 0.022 | 14.8 | 4.88 | 0.098 | 8482 |
| (g) | 4400 | 153.4 | $1.0 \times 10^6$ | 0.052 | 15.1 | 4.97 | 0.10 | 10883 |
| (h) | 4400 | 190.6 | $2.0 \times 10^7$ | 1.03 | 15.5 | 5.1 | 0.11 | 5687 |

Chebyshev Lobatto collocation nodes are adjusted such that the maximum cross-streamwise grid spacing is less than 5.4 wall units ($\Delta y^+,\ \Delta z^+ < 5.4$). The time step was fixed at $\Delta t u_b/h = 1.93$ approximately corresponding to a CFL number of 0.22. Statistics were accumulated over a time period $t_{stat}$ larger than $8000h/u_b$. The streamwise extension of the computational domain was taken as $L_x/h = 4\pi$, which is sufficiently long to allow for an adequate decay of the two-point velocity correlations [4].

As already mentioned, the numerical technique used in this paper has been extensively validated by the present authors considering isothermal flows in square ducts. In particular cases at $Re_b = 4400$ and $Re_b = 7000$ have been proved to compare quite well with both DNS reference data of Gavrilakis [4] and with experimental data obtained from LDV measurements [11] (see the recent study of Pinelli *et. al.* [12] for details). In order to validate the extension of the numerical procedure to non-isothermal conditions, we have performed numerical simulations of the same configuration as considered by Ma *et. al.* [7]. They have undertaken finite-difference-based DNS computations in low-Reynolds-number turbulent thermal duct flow with an imposed temperature difference between the vertical walls, while assuming the horizontal walls to be perfectly insulated (a different configuration from the central subject of the present contribution). In particular, we have carried out a direct comparison for cases at $Re_b = 6200$, $Gr = 10^5, 10^6, 10^7$ and $Pr = 0.7$. Figure 2 shows a comparison of the local shear stress and the local Nusselt number on the heated vertical

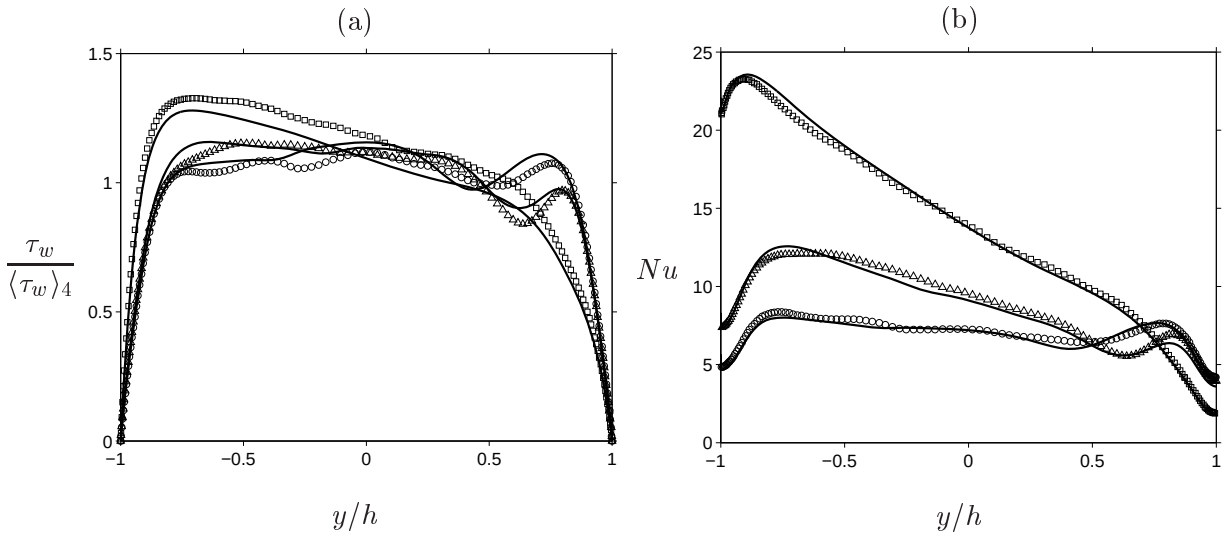


FIG. 2: The lateral variation on the heated wall ($z/h = -1$) of (a) the wall shear stress $\tau_w$ and (b) the Nusselt number $Nu$. Solid lines represent the result from the present DNS and symbols denote from Ma *et. al.*'s [7] DNS: $\circ$, $Gr = 1.0 \times 10^5$; $\triangle$, $Gr = 1.0 \times 10^6$; $\square$, $Gr = 1.0 \times 10^7$.

wall. Although small discrepancies can be observed, it can be asserted that the present results show good agreement with Ma *et al.*'s predictions. A possible explanation for the slight disagreements may be given in terms of the relatively short period of time considered by Ma *et. al.* for the accumulation of statistical data (their sampling time was 450 $u_b/H$ in contrast with the present simulations that considered more than 2000 $u_b/H$ time units). Another source of inconsistency may originate from the relatively coarser spatial resolution combined with a lower order method used by Ma *et al.*

## III. GLOBAL CHARACTERISTICS

As a first approach, in order to determine the importance of the buoyancy effects over the global behavior of both the velocity and the thermal fields, we will quantify the variations of the mean friction factor $f$ and of the mean Nusselt number $\langle Nu\rangle_2$ when increasing the value of the Richardson number. Another integral measure of the velocity field that will be considered in the analysis of $Ri$ dependence is the intensity of the mean secondary flow $U_\perp$, defined as $U_\perp = \left[(1/4h^2)\int_{-h}^{+h}\int_{-h}^{+h}(\overline{v}^2 + \overline{w}^2)\mathrm{d}y\mathrm{d}z\right]^{1/2}$.

In figures 3(a, b), the predicted values of $f$ and $\langle Nu\rangle_2$ are given as a function of $Ri$ for the two values of $Re_b$ considered in the present work. Both quantities appear to be

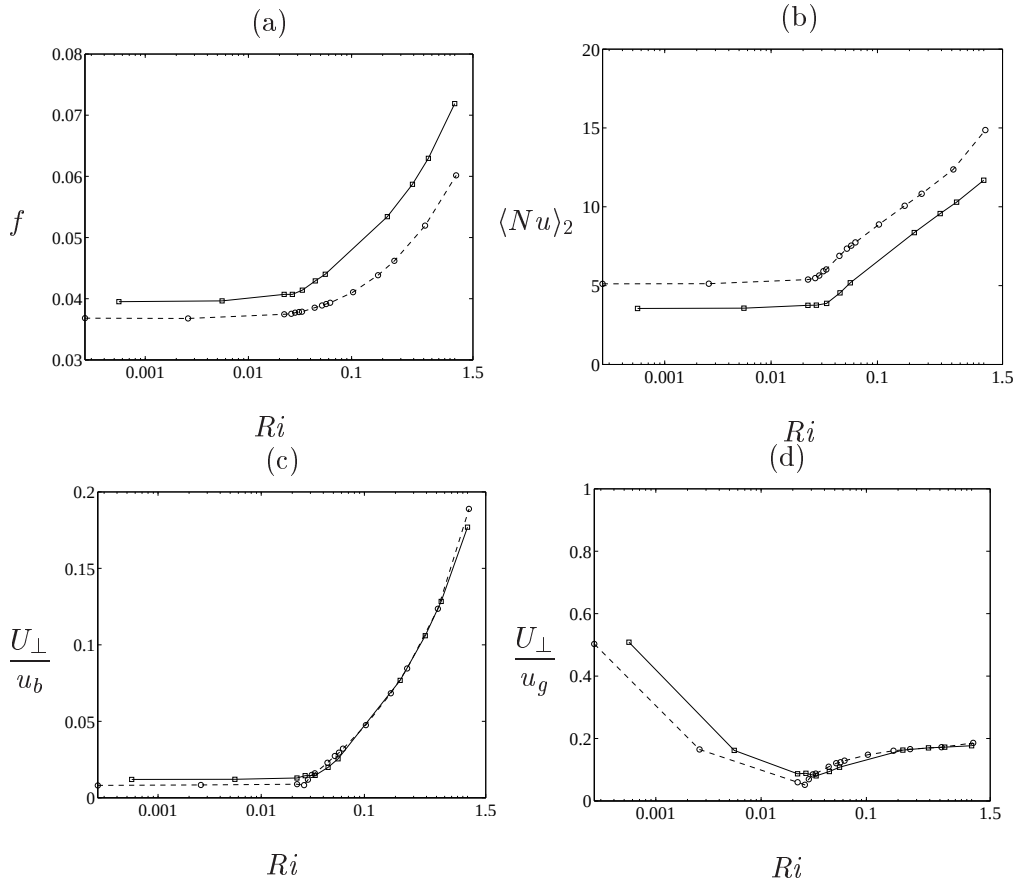


FIG. 3: The $Ri$ dependence of (a) the mean friction factor $f$ and (b) the mean Nusselt number $\langle Nu \rangle_2$, and the intensity of the mean secondary flow $U_\perp$ normalized by (c) $u_b$ and (d) $u_g$=$\sqrt{g\beta\Delta TH}$, respectively. —□—, $Re_b = 3000$; – – ○– –, $Re_b = 4400$.

increasingly affected by buoyancy effects for values of the Richardson number $Ri \gtrsim 0.025$. To better understand the behavior of the mean secondary flow intensity as a function of $Ri$, we introduce the average operator over time and streamwise direction $\overline{(\cdot)}$, and the associated decomposition $\phi(x,y,z,t) = \overline{\phi}(y,z) + \phi'(x,y,z,t)$ for all the variables. Applying the averaging operator to the momentum and temperature equations, one obtains the system of equations that governs the distribution of the mean variables:

$$\overline{v}\frac{\partial \overline{u}}{\partial y} + \overline{w}\frac{\partial \overline{u}}{\partial z} = -\frac{1}{\rho}\frac{\partial \overline{p}}{\partial x} - \frac{\partial \overline{u'v'}}{\partial y} - \frac{\partial \overline{u'w'}}{\partial z} + \nu\left(\frac{\partial^2 \overline{u}}{\partial y^2} + \frac{\partial^2 \overline{u}}{\partial z^2}\right), \tag{10}$$

$$\overline{v}\frac{\partial \overline{v}}{\partial y} + \overline{w}\frac{\partial \overline{v}}{\partial z} = -\frac{1}{\rho}\frac{\partial \overline{p}}{\partial y} - \frac{\partial \overline{v'^2}}{\partial y} - \frac{\partial \overline{v'w'}}{\partial z} + \nu\left(\frac{\partial^2 \overline{v}}{\partial y^2} + \frac{\partial^2 \overline{v}}{\partial z^2}\right) + g\beta(\overline{T} - T_0), \tag{11}$$

$$\overline{v}\frac{\partial \overline{w}}{\partial y} + \overline{w}\frac{\partial \overline{w}}{\partial z} = -\frac{1}{\rho}\frac{\partial \overline{p}}{\partial z} - \frac{\partial \overline{v'w'}}{\partial y} - \frac{\partial \overline{w'^2}}{\partial z} + \nu\left(\frac{\partial^2 \overline{w}}{\partial y^2} + \frac{\partial^2 \overline{w}}{\partial z^2}\right) \tag{12}$$

and that for the mean temperature

$$\overline{v}\frac{\partial\overline{T}}{\partial y}+\overline{w}\frac{\partial\overline{T}}{\partial z} \;=\; -\frac{\partial\overline{v'T'}}{\partial y}-\frac{\partial\overline{w'T'}}{\partial z}+\kappa\left(\frac{\partial^2\overline{T}}{\partial y^2}+\frac{\partial^2\overline{T}}{\partial z^2}\right). \tag{13}$$

In the case of finite $Ri$, when the buoyancy term may be comparable with the mean-flow convection terms and all other terms are of lesser magnitude (i.e., $\overline{v}\frac{\partial\overline{v}}{\partial y}\sim\overline{w}\frac{\partial\overline{v}}{\partial z}\sim g\beta(\overline{T}-T_0)$), equation (11) provides for the balance:

$$\frac{U_\perp^2}{H}\;\sim\; g\beta\Delta T,\;\;\text{or equivalently}\;\; U_\perp\sim u_g=\sqrt{g\beta\Delta TH}, \tag{14}$$

In figures 3(c, d), $U_\perp$ is shown as a function of $Ri$, when normalized by $u_b$ and $u_g$ respectively. The non-dimensional velocity scale $U_\perp/u_b$ associated with the mean secondary flow increases with $Ri$ at $Ri\gtrsim 0.025$, thus confirming that this value of $Ri\sim 0.025$ is a threshold for buoyancy effects to come into play. Indeed, for values of $Ri\gtrsim 0.25$, the intensity of the mean secondary flow starts to scale with $u_g$, thus implying that the secondary flow is predominantly driven by buoyancy force. Therefore, the mean flow behaviors described by figure 3 allow for introducing three different flow regimes according to the value of $Ri$:

*Regime* (i) $0\leq Ri\lesssim 0.025$, buoyancy effects are negligible and therefore the mean secondary flow is solely determined by turbulence;

*Regime* (ii) $0.025\lesssim Ri\lesssim 0.25$, intermediate *equilibrium* regime in which both turbulence and buoyancy effects determine the character of the mean secondary flow;

*Regime* (iii) $Ri\gtrsim 0.25$, buoyancy dominated regime in which thermal convection determines the character of the secondary flow.

Next, we discuss the proper scalings of the r.m.s. fluctuations of both velocity and temperature fields. To this end we consider again the set of averaged equations (10, 11, 12 and 13), also introducing three magnitudes to be used as a measure the intensity of the r.m.s. fluctuations of the variables. In particular, the intensity of the cross stream-wise r.m.s. fluctuations will be assessed by the integral velocity value $U_{\mathrm{rms}\perp}\equiv\left[(1/4h^2)\int_{-h}^{+h}\int_{-h}^{+h}\overline{(v'^2)}\mathrm{d}y\mathrm{d}z\right]^{1/2}$. Analogously, to characterize the stream-wise r.m.s. fluctuations the value of $U_{\mathrm{rms}}\equiv\left[(1/4h^2)\int_{-h}^{+h}\int_{-h}^{+h}\overline{u'^2}\mathrm{d}y\mathrm{d}z\right]^{1/2}$ will be used. Finally, the r.m.s. fluctuation of the temperature field will be characterized by the value of $T_{\mathrm{rms}}\equiv\left[(1/4h^2)\int_{-h}^{+h}\int_{-h}^{+h}\overline{T'^2}\mathrm{d}y\mathrm{d}z\right]^{1/2}$. Firstly, we focus on the scaling of $U_{\mathrm{rms}\perp}$ by considering equation (11). From the latter, it turns out that

there exist two possible balances between terms. The first one is between the mean-flow and the turbulent convection terms (i.e., $\overline{v}\dfrac{\partial \overline{v}}{\partial y} \sim \overline{w}\dfrac{\partial \overline{v}}{\partial z} \sim \dfrac{\partial \overline{v'^2}}{\partial y} \sim \dfrac{\partial \overline{v'w'}}{\partial z}$), which when using the result in (14) leads to:

$$u_g^2 \sim U_{\mathrm{rms}\perp}^2 \;\text{ or equivalently }\; U_{\mathrm{rms}\perp} \sim u_g. \tag{15}$$

The other possible balance concerns the equilibrium between the turbulent convection terms and the viscous ones (i.e., $\dfrac{\partial \overline{v'w'}}{\partial y} \sim \dfrac{\partial \overline{w'^2}}{\partial z} \sim \nu\dfrac{\partial^2 \overline{w}}{\partial y^2} \sim \nu\dfrac{\partial^2 \overline{w}}{\partial z^2}$), providing for the estimate:

$$U_{\mathrm{rms}\perp}^2 \sim \nu\frac{u_g}{H} \;\text{ or equivalently }\; U_{\mathrm{rms}\perp} \sim \sqrt{u_\nu u_g}, \tag{16}$$

where $u_\nu = \nu/H$ is the viscous velocity scale. Figure 4(a, b) shows the reference value of the cross-streamwise r.m.s. velocity normalized with $u_g$ and $\sqrt{u_\nu u_g}$ as a function of $Ri$, respectively. $U_{\mathrm{rms}\perp}$ could be seen to scale with $\sqrt{u_\nu u_g}$ rather than $u_g$. M.U: is the scaling really convincing? I mean, there is not a huge difference between the collapse when using the two different scales. perhaps soften the statement a little...

Next, we discuss the likely scaling for the streamwise r.m.s. velocity $U_{\mathrm{rms}}$. Again, the mean momentum equation in the streamwise direction (10) suggests two possible balances. The first one concerns the equilibrium between the mean-flow and the turbulent convection terms (i.e.,$\overline{v}\dfrac{\partial \overline{u}}{\partial y} \sim \overline{w}\dfrac{\partial \overline{u}}{\partial z} \sim \dfrac{\partial \overline{u'v'}}{\partial y} \sim \dfrac{\partial \overline{u'w'}}{\partial z}$), leading to the estimate $u_g u_b \sim U_{\mathrm{rms}} U_{\mathrm{rms}\perp}$. Using relation (16), we obtain the estimate

$$U_{\mathrm{rms}} \;\sim\; u_b\sqrt{\frac{u_g}{u_\nu}}. \tag{17}$$

On the other hand, if the balance between the turbulent convection and viscous terms is supposed to take place (i.e., $\dfrac{\partial \overline{u'v'}}{\partial y} \sim \dfrac{\partial \overline{u'w'}}{\partial z} \sim \nu\dfrac{\partial^2 \overline{u}}{\partial y^2} \sim \nu\dfrac{\partial^2 \overline{u}}{\partial z^2}$), the following relation holds:

$$U_{\mathrm{rms}}\sqrt{u_\nu u_g} \sim u_\tau^2, \;\text{ or equivalently }\; U_{\mathrm{rms}} \sim \frac{u_\tau^2}{\sqrt{u_\nu u_g}}, \tag{18}$$

where, the last estimate is obtained by using again the relation (16). Figure 5(a, b) shows the reference values of the streamwise r.m.s. velocity as a function of $Ri$, normalized by $u_b\sqrt{u_g/u_\nu}$ and $u_\tau^2/\sqrt{u_\nu/u_g}$ respectively. $U_{\mathrm{rms}}/(u_b\sqrt{u_g/u_\nu})$ monotonically decreases with increasing $Ri$, while $U_{\mathrm{rms}}/(u_\tau^2/\sqrt{u_\nu/u_g})$ increases. The latter can be seen to approach the upper limit at larger $Ri$, suggesting that $U_{\mathrm{rms}}$ might scale according to

$u_\tau^2/\sqrt{u_\nu/u_g}$ rather than $u_b\sqrt{u_g/u_\nu}$. M.U: same as above -- the scaling seems little convincing, i.e. both scales make curves similarly collapse!

Finally, to determine the probable scaling for the temperature r.m.s., we consider the two possible balances offered by equation (13). The balance between the mean-flow and the turbulence-convection terms, (i.e., $\overline{v}\dfrac{\partial\overline{T}}{\partial y} \sim \overline{w}\dfrac{\partial\overline{T}}{\partial z} \sim \dfrac{\partial\overline{v'T'}}{\partial y} \sim \dfrac{\partial\overline{w'T'}}{\partial z}$), yields

$$u_g\Delta T \sim U_{\mathrm{rms}\perp}T_{\mathrm{rms}}, \text{ or equivalently } T_{\mathrm{rms}} \sim \Delta T\sqrt{\frac{u_g}{u_\nu}}. \tag{19}$$

From the other possible balance between the turbulent convection and the diffusive terms (i.e.,$\dfrac{\partial\overline{v'T'}}{\partial y} \sim \dfrac{\partial\overline{w'T'}}{\partial z} \sim \kappa\dfrac{\partial^2\overline{T}}{\partial y^2} \sim \kappa\dfrac{\partial^2\overline{T}}{\partial z^2}$), we obtain

$$U_{\mathrm{rms}\perp}T_{\mathrm{rms}} \sim u_\tau T_\tau, \text{ or equivalently } T_{\mathrm{rms}} \sim T_\tau\frac{u_\tau}{\sqrt{u_\nu u_g}}, \tag{20}$$

where $T_\tau = (1/u_\tau)\kappa\langle\partial T/\partial y\rangle_2$ denotes the friction temperature. Figure 6 shows the dependence of the r.m.s. temperature from $Ri$ when normalized by $\Delta T\sqrt{u_g/u_\nu}$ and $T_\tau u_\tau/\sqrt{u_\nu u_g}$ respectively. Although $T_{\mathrm{rms}}/(\Delta T\sqrt{u_g/u_\nu})$ monotonically decreases with increasing $Ri$, $T_{\mathrm{rms}}/(T_\tau u_\tau/\sqrt{u_\nu u_g})$ stays around a roughly constant value at large $Ri$, implying that the r.m.s. of the temperature field scale with $T_\tau u_\tau/\sqrt{u_\nu u_g}$ rather than $\Delta T\sqrt{u_g/u_\nu}$. M.U: here i am lost. can you explain what is meant by scaling?

The above results have indicated that the r.m.s. of the cross-streamwise velocity, the streamwise velocity and the temperature, $U_{\mathrm{rms}\perp}$, $U_{\mathrm{rms}}$ and $T_{\mathrm{rms}}$, might scale, respectively, with $\sqrt{u_\nu u_g}$, $u_\tau^2/\sqrt{u_\nu/u_g}$ and $T_\tau u_\tau/\sqrt{u_\nu u_g}$, all of which have been obtained from the balances between turbulence convection and molecular diffusion of momentum or heat.

## IV. MEAN VELOCITY AND TEMPERATURE

The cross-sectional distributions of the mean streamwise and cross-streamwise velocity at the various combinations of Grashof number and Reynolds number values (as indicated in table I) are shown in Fig.7. At the smallest $Ri$, the secondary flow vectors exhibit the usual symmetric eight-vortex patterns with respect to the wall and the corner bisectors, being typical of the turbulence-driven cross-flow as shown in Fig. 7(a, e). At slightly larger values ($Ri = 0.022$), roughly corresponding to the border between *regime* (i) and (ii), the eight-vortex secondary flow is still observed, both for $Re_b = 3000, 4400$, but at the higher Reynolds number (Fig. 7f) the clockwise mean secondary vortices are weakened due to the

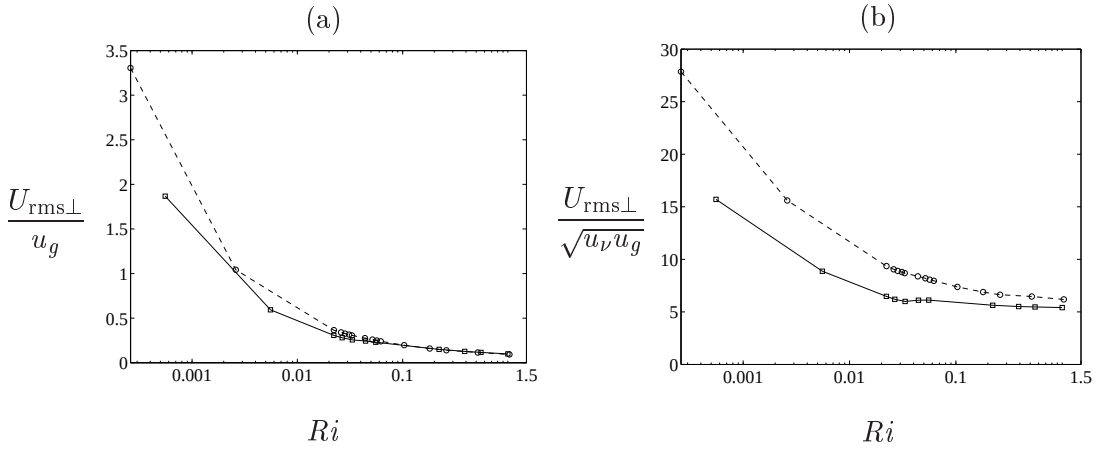


FIG. 4: The $Ri$ dependence of the reference cross-streamwise r.m.s. velocity $U_{\mathrm{rms}\perp}$ normalized by (a) $u_g$ and (b) $\sqrt{u_\nu u_g}$. —□—, $Re_b = 3000$; – – ∘ – –, $Re_b = 4400$.

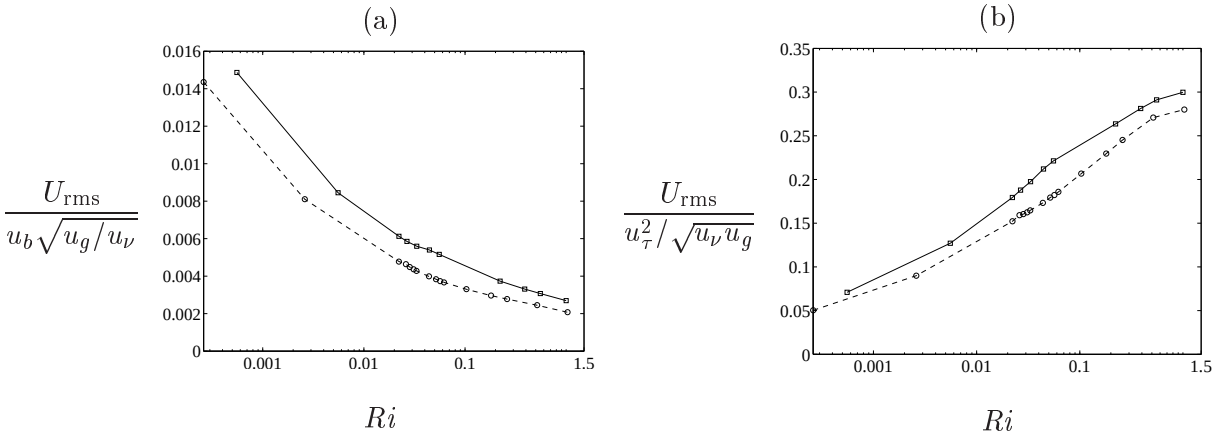


FIG. 5: The $Ri$ dependence of the reference streamwise r.m.s. velocity $U_{\mathrm{rms}}$ normalized by (a) $u_b\sqrt{u_g/u_\nu}$ and (b) $u_\tau^2/\sqrt{u_\nu u_g}$. —□—, $Re_b = 3000$; – – ∘ – –, $Re_b = 4400$.

buoyancy effect, so that the symmetries with respect to the wall and corner bisectors are broken.

As $Ri$ is further increased (*regime* (ii)), the large-scale circulation around the duct center acts to push four pairs of counter-rotating mean secondary vortices towards the corners, so that the four clockwise vortices of the counter-rotating pairs disappear (Fig. 7(c, g)), and eventually (*regime* (iii)) just two counter-clockwise vortices near the upper-left and lower-right corners remain significant (Fig. 7(d, h)). Note that the symmetry of the present flow system allows the large-scale convection with the opposite-signed rotation to that in Fig. 7(c, d, g, h), but in this paper only the case of the clockwise circulation is shown.

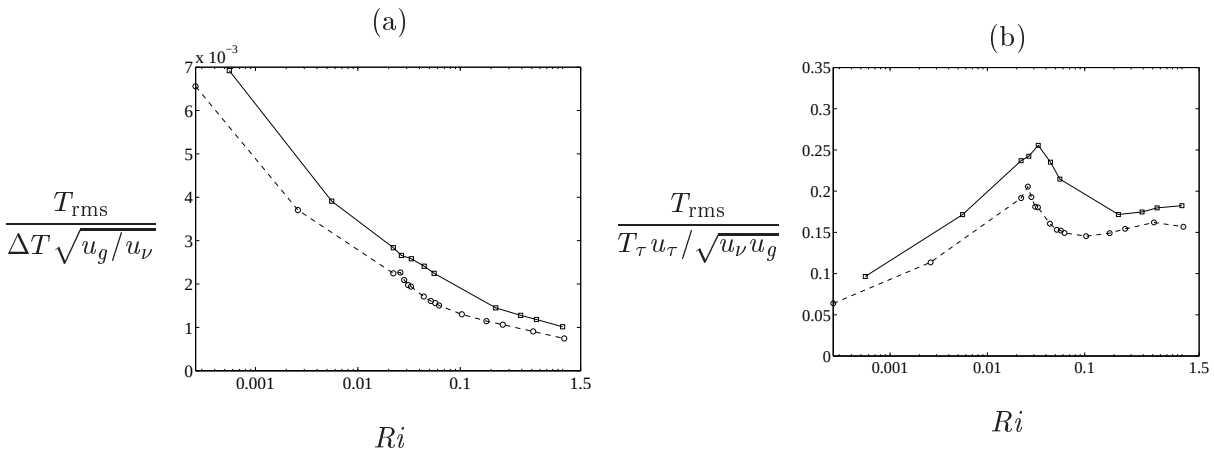


FIG. 6: The $Ri$ dependence of the reference r.m.s. temperature $T_{\rm rms}$ normalized by (a) $\Delta T\sqrt{u_g/u_\nu}$ and (b) $T_\tau u_\tau/\sqrt{u_\nu u_g}$. —□—, $Re_b = 3000$; – – ∘ – –, $Re_b = 4400$.

The mean streamwise velocity is also shown by iso-lines in Fig. 7. At $Ri \lesssim 0.025$, i.e., *regime* (i), four pairs of the counter-rotating mean vortices with the cross-streamwise velocity scaling with $u_b$ and so independent of $Ri$ (see Fig. 3(c)) transport the relatively high (or low) streamwise momentum toward the duct corner (or the duct center) along the corner bisector (or the wall bisector). As a consequence, the iso-contours of the mean streamwise velocity are denser in the corner regions, implying that the wall shear is stronger near the corner than the wall bisector. At $Ri \gtrsim 0.025$ (*Regime* (ii, iii)), on the other hand, the large-scale circulation of the velocity scale being larger for higher $Ri$ and eventually comparable with the order of $u_g$ (see Fig. 3 (c, d)) plays a crucial role in the transfer of the high streamwise momentum toward the wall, so that the iso-contours are now much denser near the walls except for the corner regions. This momentum transfer by the large-scale circulation can enhance the wall friction with increasing $Ri$, as shown in Fig. 3 (a).

The cross-sectional distributions of the mean temperature are shown in Fig. 8. At smaller $Ri$ (*regime* (i)) the turbulence-driven four pairs of counter-rotating mean vortices induce a cross-streamwise heat transfer, and thus in Fig. 8 (a, b, e, f) we can see the corrugation of the iso-therms caused by the mean vortices. At higher $Ri$ (*regime* (ii, iii)), the buoyancy-driven large-scale circulation also plays a crucial role in the heat transfer. The roughly uniform temperature distribution around the duct center in Fig. 8 (d, h) is the outcome of the large-scale heat transport and subsequent turbulence diffusion (cf. the spiral iso-therms under the action of only molecular diffusion for a comparable value of $Gr$

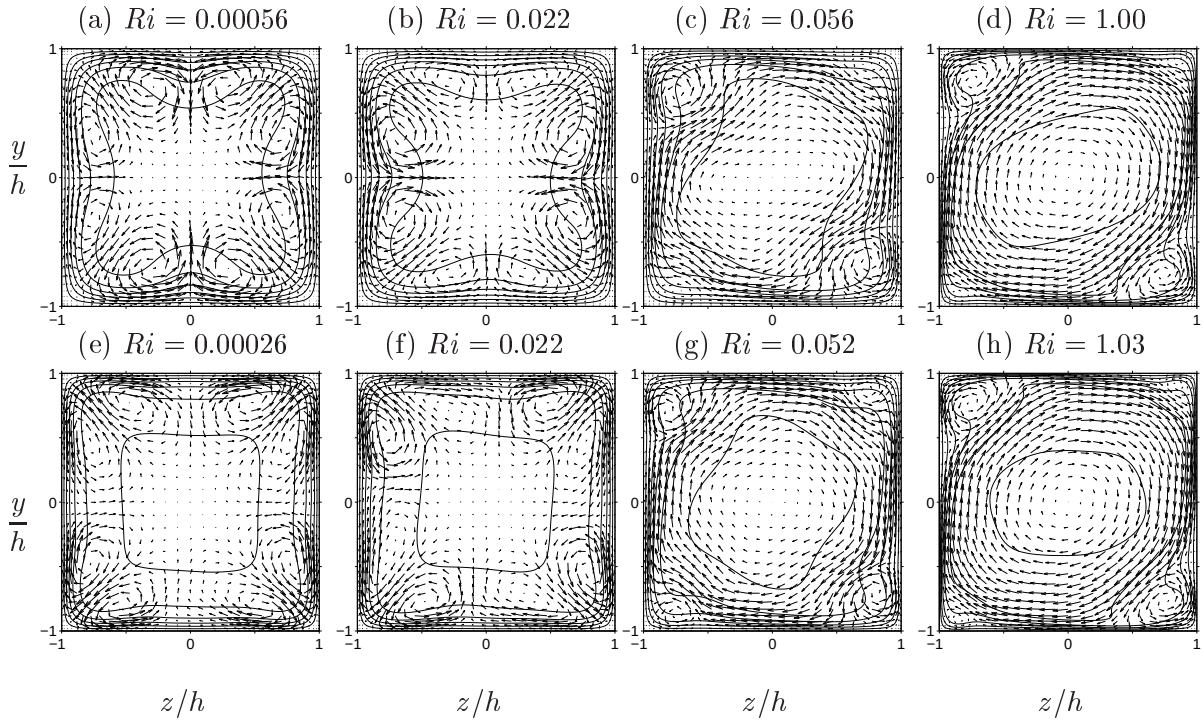


FIG. 7: Cross-sectional distributions of the mean streamwise and cross-streamwise velocity. (a-d) $Re_b = 3000$, (e-h) $Re_b = 4400$. (a) $Gr = 5.0 \times 10^3$, (b) $Gr = 2.0 \times 10^5$, (c) $Gr = 5.0 \times 10^5$, (d) $Gr = 9.0 \times 10^6$, (e) $Gr = 5.0 \times 10^3$, (f) $Gr = 4.3 \times 10^5$, (g) $Gr = 1.0 \times 10^6$, (h) $Gr = 2.0 \times 10^7$. Mean streamwise velocity is represented by iso-lines with increment 0.2 $u_b$ and mean cross-streamwise velocity is shown by vectors. The maximum values of the vectors, $\max\{\sqrt{\overline{v}^2 + \overline{w}^2}\}/u_b$, are (a) 0.024, (b) 0.028, (c) 0.029, (d) 0.145, (e) 0.020, (f) 0.021,(g) 0.027, (h) 0.15, respectively.

in Fig. 9 (a)). M.U.: the previous statement strikes me. Actually what I see on the figure is that the gradients near the center do not change so much, but rather do they rotate more towards the horizontal with increasing Ri!

As discussed above for the momentum transfer, the iso-therms are much denser near the (top and bottom) walls because of the large-scale circulation, enhancing the wall heat transfer as shown in Fig. 3 (b).

M.U.: At this point you should motivate your little detour into 2D better. To me it seemed to drop out of the sky. Although what we observed above is turbulent mixed convection, the cross-stream motion at high $Ri$ is expected to be traced to buoyancy-driven two-dimensional flow without axial turbulent flow. Therefore we shall discuss the relevance of the mean secondary flow observed at higher $Ri$

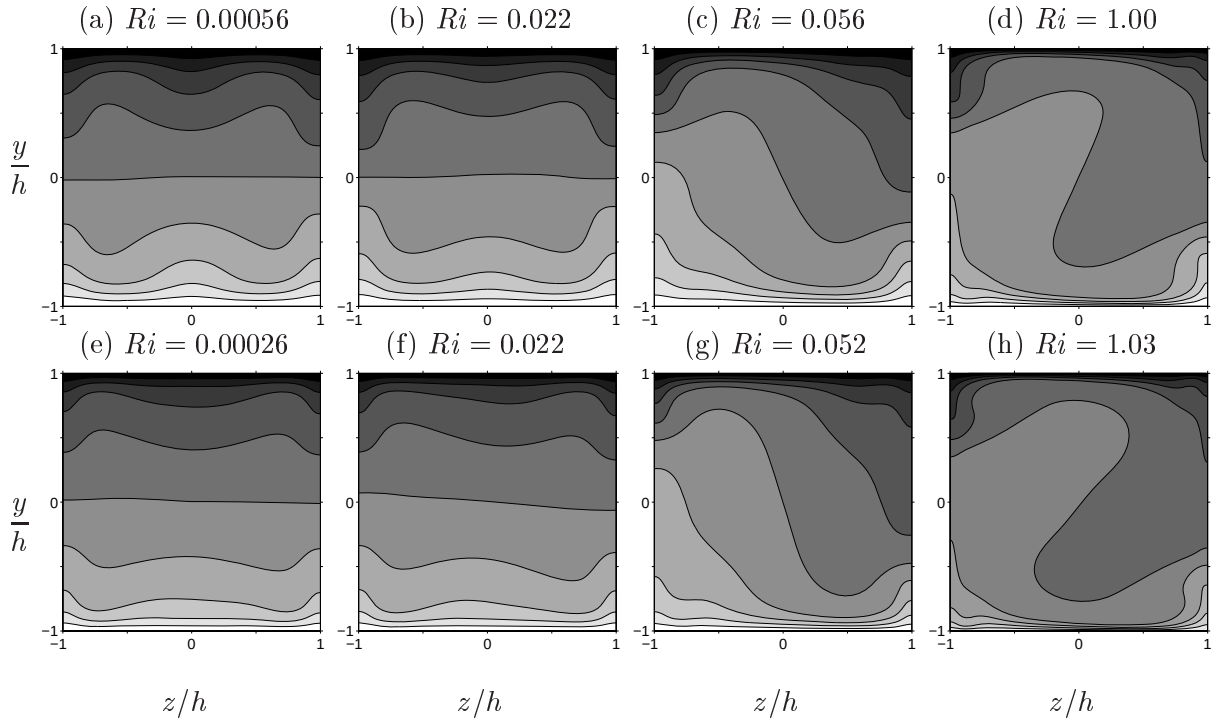


FIG. 8: The same as Fig. 7 but for the mean temperature represented by gray scales in the interval of 0.1 $\Delta T$. (a-d) $Re_b = 3000$, (e-h) $Re_b = 4400$.

(or $Gr$) to two-dimensional thermal convection in a square container heated from below. The two-dimensional thermal convection is numerically examined at the same value of the Grashof number, $Gr = 1.0 \times 10^6$, as that for the case of $Re_b = 4400$ and $Ri = 0.052$ in Fig. 7 (g) (*regime* (ii)). In the computation, the Fourier mode of the cross-streamwise velocity and the temperature for null streamwise wavenumber is decoupled from the other Fourier modes to represent the two-dimensional laminar flow under the same boundary conditions on the walls. Figure 9 (a) shows the velocity and temperature fields of the two-dimensional laminar thermal convection. At this value of Grashof number, a steady flow state is observed and it is characterized in terms of the large-scale circulation and the two additional small-scale vortices in the upper-left and lower-right corner regions. Note that the thermal convection with the same sense of rotation as before is shown in the figure. The streamfunction $\psi$ of the thermal convection is shown in Fig. 9 (b). The value of the streamfunction on the walls is taken to be zero, so that its positive (or negative) value may represent clockwise (or counter-clockwise) rotational motion. Significantly negative $\psi$ appears neither near the upper-right corner nor near the lower-left corner, implying that the

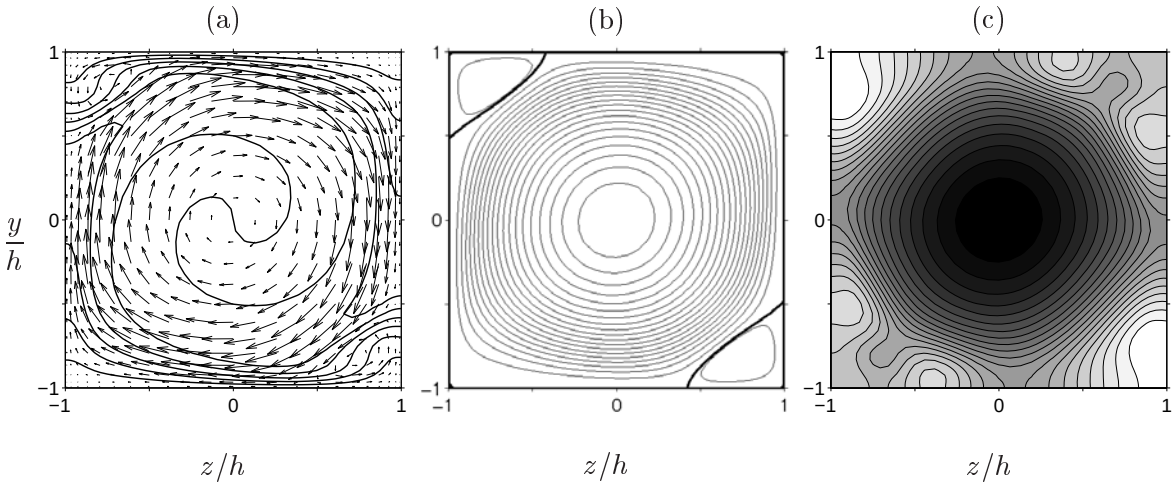


FIG. 9: The steady two-dimensional thermal convection pattern at $Gr = 1.0 \times 10^6$. (a) The cross-streamwise velocity and the temperature represented, respectively, by vectors and the contour lines in the interval of 0.1 $\Delta T$. (b) The streamfunction $\psi$. The bold solid line represents the contour of $\psi = 0$. The boundaries are also $\psi = 0$. (b) The cross-streamwise distribution of pressure: (white), the highest pressure; (black), lowest pressure.

small-scale upper-right and lower-left mean vortices observed in Fig. 7 (c, g) (*regime* (ii)) are turbulence-driven while the upper-left or lower-right mean vortices are buoyancy-driven. M.U.: cannot follow the argument you are laying out next... Let us briefly discuss why only the upper-left and lower-right vortices appear in the thermal convection. Fluids close to the horizontal lower (or upper) wall are heated (or cooled), but their velocity towards the vertical left (or right) wall is retatively small because the fluids thereon cannot be directly accelerated by buoyancy under the constraint of an impermeable wall. Hot (or cold) fluids near the vertical left (or right) wall can, on the other hand, be accelerated by buoyancy, so that their velocity towards the horizontal upper (or lower) wall is larger. As a consequence, 'splashing' of the high-velocity fluids on the horizontal wall would increase the pressure thereon (see Fig. 9 (c)) high enough to form separation bubbles or vortices in the upper-left and lower-right corner regions.

In order to demonstrate the quantitative difference between the turbulence- and the buoyancy-driven corner vortices in Fig. 7, we show the $Ri$-dependence of the positions of the extrema of the mean streamwise vorticity $\overline{\omega}_x$ in Fig. 10 (see Fig. 14 (a, c) for the spatial distribution of $\overline{\omega}_x$ at $Ri = 0.052$, 1.03 and $Re = 4400$). Because the mean secondary flow in

a square duct obtained from the Boussinesq approximation has a 180° rotational symmetry with respect to the duct center axis, we have only shown the positions of the lower-left and lower-right vortices. As for the small-scale lower-left (counter-clockwise) vortex, the distance $s_z$ from the side wall ($z = -h$) to the position of the minimum of the mean streamwise vorticity $\overline{\omega_x}$ normalized by the duct half width $h$ and the friction length $\nu/u_\tau$ is shown in Fig. 10 (a) and (c), respectively. The distance $s_y$ from the bottom wall ($y = -h$) to the position of the minimum of $\overline{\omega_x}$ for the lower-right vortex is normalized by $h$ and friction length $\nu/u_\tau$ as shown in Fig. 10 (b, d), respectively.

M.U.: again, I am not so covinced by the following scaling plots. Also, I think you should be referring to figures 10 (a) and (c), instead of twice to 10 (c). We can see in Fig. 10 (c) that the position of the lower-left vortex, which does not appear in the laminar convection (see Fig. 9), scales with the friction length rather than the duct width (Fig. 10 (c)). Such a scaling property has also been observed for turbulence-driven mean secondary flow vortices in an isothermal duct, which are a direct consequence of instantaneous near-wall streamwise vortices [12]. The generation mechanism of the lower-left and upper-right (turbulence-driven) vortices will be discussed in terms of instantaneous coherent vortices in section VI.

The position of the lower-right vortex, which is also observed in the laminar convection (Fig. 9 (b)), can be seen to scale with the duct width rather than the friction length in Fig. 10 (b). This is a scaling property of thermal convection and is contrasted with the above near-wall scaling of the turbulence-driven lower-left vortex. M.U.: is there a literature reference for this scaling in thermal convection?

## V. STREAMWISE R.M.S. VELOCITY AND R.M.S. TEMPERATURE

Figure 11 shows the cross-sectional distributions of the streamwise r.m.s. velocity $\sqrt{\overline{u'^2}}$. As $Ri$ increases, the intense region of the streamwise r.m.s. velocity shifts from the wall bisector towards the corners (Fig. 11(c, g)) through the sweeping effects of the large-scale circulation. As $Ri$ further increases (Fig. 11(d, h)), the two intense regions are separated from the side walls because of the flow detachment induced by buoyancy-driven circulation (see Fig. 9). At $Ri \sim 1.0$ the streamwise r.m.s. velocity is relatively low around the centers of the buoyancy-driven small-scale secondary flow vortices in the upper-left and lower-right corner

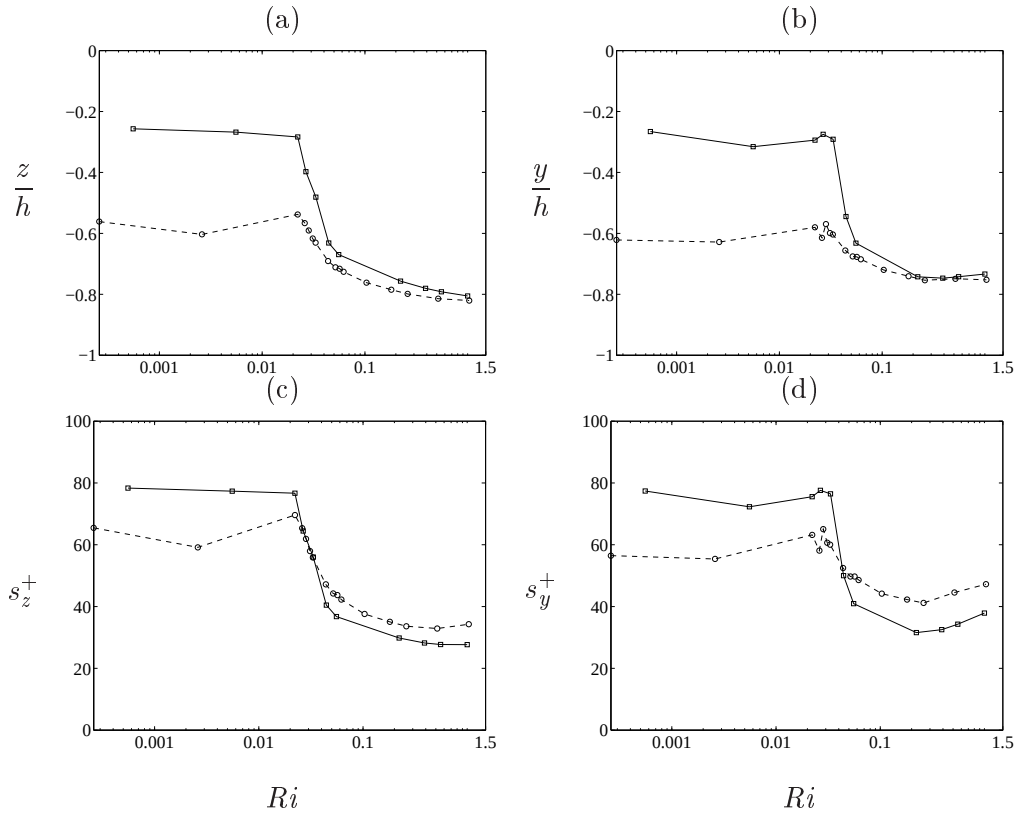


FIG. 10: The $Ri$ dependence of the position of the local minimum of the mean streamwise vorticity $\overline{\omega_x}$ for (a), (c) the lower-left and (b), (d) the lower-right mean secondary vortex in Fig. 7. (a), (b) the position normalized with the duct half width. (c), (d) the position normalized with the friction length. —□—, $Re_b = 3000$; – – ○ – –, $Re_b = 4400$.

regions, which correspond to 'separation bubbles'. M.U.: wouldn't it be better to discuss directly the turbulent kinetic energy here? Although not shown, the cross-streamwise r.m.s. velocity has also been observed to be small in the separation bubbles, and thus the bubbles could be characterized by a roughly steady quiescent state. On the other hand, large values of the streamwise r.m.s. velocity can be observed in the upper-right and lower-left corner regions where the turbulence-driven small-scale mean secondary flow vortices exist.

Figure 12 shows the cross-sectional distributions of the r.m.s. temperature $\sqrt{\overline{T'^2}}$. In contrast to the r.m.s. velocity, large temperature fluctuations can be seen to appear in the central region of the duct at smaller $Ri$ (Fig. 12(a, b)) because there is the mean temperature gradient in the vertical direction (see Fig. 8 (a, b, e, f)), across which the turbulent fluid moves up and down. At higher $Ri$, on the other hand, the temperature fluctuation is very

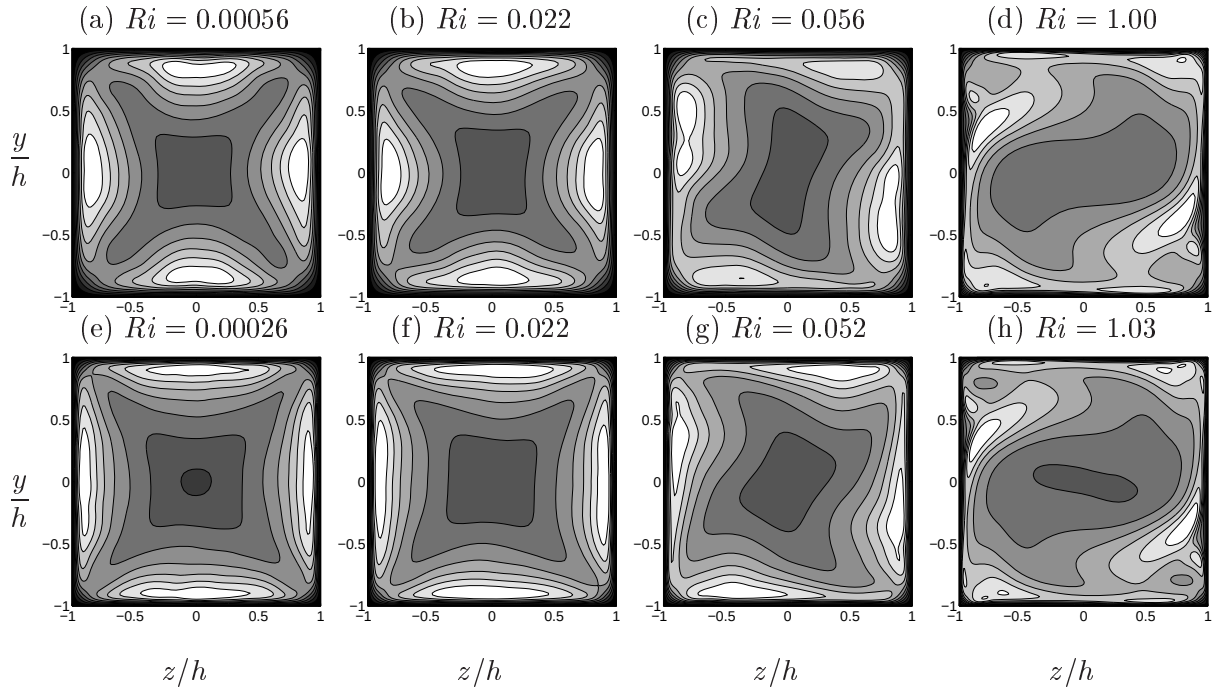


FIG. 11: The same as Fig. 7 but for the streamwise r.m.s. velocity $\sqrt{\overline{u'^2}}$ represented in gray scales (white and black shows the maximum and minimum value, respectively). The maximum values of , $\sqrt{\overline{u'^2}}/u_b$, are (a) 0.66, (b) 0.67, (c) 0.66, (d) 0.63, (e) 0.65, (f) 0.64,(g) 0.61, (h) 0.63, respectively. (a-d) $Re_b = 3000$, (e-h) $Re_b = 4400$.

small in the central region. This is because the stirring effect of the large-scale circulation and subsequent diffusion for the temperature smooth out the mean temperature distribution around the duct center, leading to the small temperature fluctuation around the duct center.

## VI. BUOYANCY EFFECTS ON FLOW STRUCTURES

Figure 13 shows the snapshots of the instantaneous flows at $Re_b = 4400$ for three values of $Ri = 0.00026$, 0.052 and 1.03, which belong to the *regime* (i), (ii) and (iii), respectively. The low-velocity streaks are visualized by the corrugated gray iso-surface at the level of 0.6 $u_b$ and the streamwise vortices are visualized by the tubular iso-surfaces of the second invariant of the velocity gradient tensor [13] at the level of 0.03 $u_\tau^4/\nu^2$, which are lighted or shaded with the sign of the streamwise vorticity (the light objects are clockwise vortices and the dark objects are counter-clockwise vortices). The visualized streaks and vortices can be

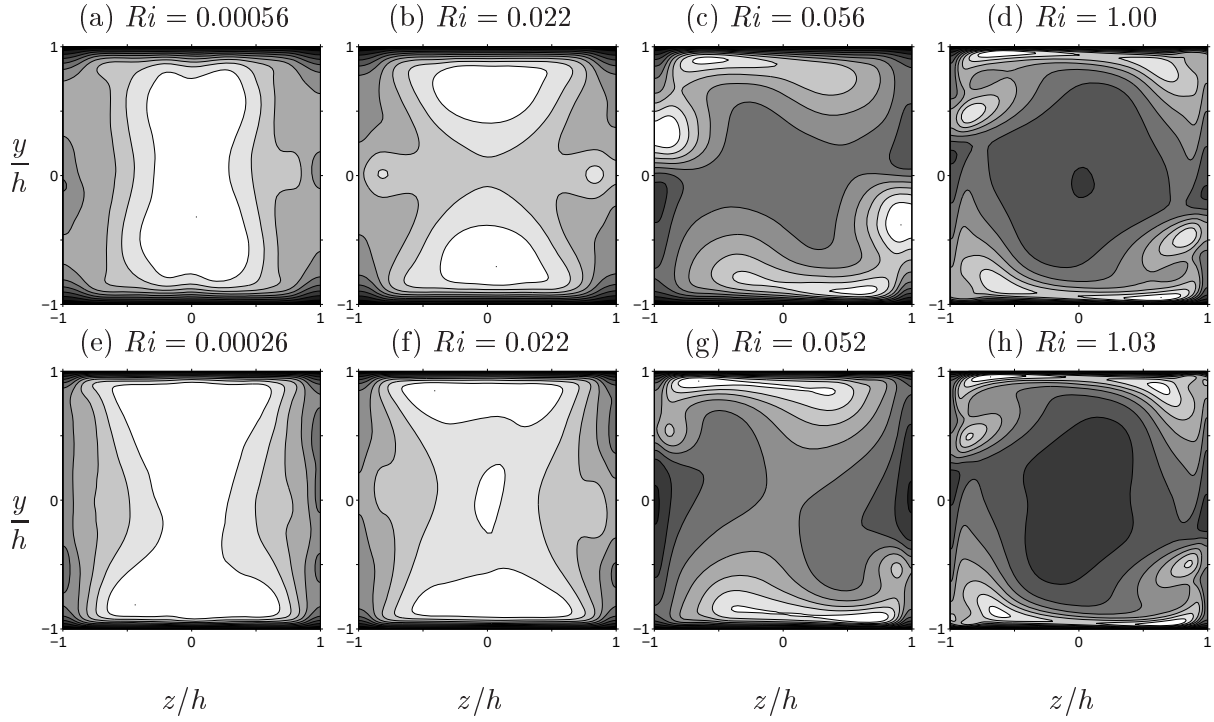


FIG. 12: The same as Fig. 7 but for the r.m.s. temperature $\sqrt{\overline{T'^2}}$ represented in gray-scale (white and black shows the maximum and minimum value, respectively). The maximum values of , $\sqrt{\overline{T'^2}}/\Delta T$, are (a) 0.20, (b) 0.20, (c) 0.23, (d) 0.23, (e) 0.19, (f) 0.19,(g) 0.21, (h) 0.23, respectively. (a-d) $Re_b = 3000$, (e-h) $Re_b = 4400$.

seen to be swept towards the corner by the large-scale circulation induced by the buoyancy force (cf. Figs. (a, b)). The shift of the intense region of the streamwise r.m.s. velocity and r.m.s. temperature towards the corners in Fig. 11 and 12 is attributed to this sweeping effect on these near-wall structures by the buoyancy-driven circulation. The streamwise vortices exist even at $Ri = 1.03$ and, under the action of the wall-parallel motion induced by the large-scale circulation, the streaks and vortices exhibit the tendency to align in the direction which is deviated from the streamwise direction in the spanwise direction.

### A. Streamwise vortices

Now, we investigate the relation between the instantaneous quasi-streamwise vortices and the mean secondary flows. To quantitatively discuss it, we define the cross-sectional center of the streamwise vortices as the position of a local pressure minimum with the swirl

condition $D < 0$, where $D$ is the discriminant of the velocity gradient tensor in the cross-plane, i.e. $D = (\partial v/\partial y - \partial w/\partial z)^2/4 + (\partial v/\partial z)(\partial w/\partial y)$ [14]. We do not need to set any thresholds to the extraction of the vortex centers in this definition. M.U.: why don't you need any threshold here? Remember we did need one in isothermal flow. We plot the p.d.f.s of the positions of the centers of the clockwise and counter-clockwise vortices with positive and negative streamwise vorticity, respectively, in Fig. 14(a, b) and Fig. 14(d, e). The p.d.f.s are computed by taking into account the 180°-rotational symmetry with respect to the duct center axis to increase the number of realizations. The result is then replicated on the upper and lower half for convenience. The corresponding mean streamwise vorticity is shown in Fig. 14(c) and Fig. 14(f).

In the case of $Re_b = 4400$ and $Ri = 0.052$, corresponding to *regime* (ii) in which turbulence- and buoyancy-driven secondary flow is observed, the positions of the maximum p.d.f.s for the instantaneous counter-clockwise vortices (Fig. 14(b)) in all the corner regions can be seen to be consistent with those of the negative extrema of (is this correct?) the mean streamwise vorticity (Fig. 14(c)). The same is not true for the instantaneous clockwise vortices (Fig. 14(a)) which do not frequently appear near the positions of the positive extrema of the streamwise-vorticity. Except in the corner regions we cannot see remarkable differences in the p.d.f.s for the clockwise and counter-clockwise vortices which mostly cancel out each other. These results imply that the instantaneous streamwise coherent vortices of the opposite sense of rotation to the large-scale circulation play a role in the generation of the four mean secondary corner vortices. As will be discussed below, under the effect of the large-scale circulation as well as the geometrical constraint in the corner regions, the instantaneous vortices of the counter-clockwise (is this correct?) sense of rotation have a preferential location near the corner, so that the mean secondary corner vortices would appear as their statistical footprint.

Above we have observed significant differences between the patterns of the mean secondary flow in the *regimes* (i) and (ii) (cf. Fig 7 (a, b, e, f) and (c, g)). M.U.: I do not get this following paragraph: This difference would be ascribed to a marked contrast of dynamical behavior of the instantaneous vortices in the *regime* (ii) with the *regimes* (i) in which just the geometrical constraint in the corner regions remain to accommodate the coherent vortices of both senses of rotation, leading to the appearance of the mean secondary flow exhibiting four pairs of counter-rotating vortices (see Uhlmann *et al* [5]).

In the case of $Ri = 1.03$ allocated to the *regime* (iii) in which the buoyancy-driven secondary flow is dominant, the positions of the maximum p.d.f.s for the instantaneous counter-clockwise vortices (Fig. 14(e) in the upper-right and lower-left corner regions are still consistent with those of the weak extreme of the mean streamwise vorticity (Fig. 14(f)); however, they can be seen to shrink to the close vicinity of the corresponding corners, implying that the instantaneous vortices are confined to the smaller regions for larger $Ri$ through the sweeping effect of the large-scale circulation, as will be discussed below. Therefore, the mean secondary vortices cannot be seen clearly in the upper-right and lower-left corner regions in Fig. 7(d, h). On the other hand, the positions of the maximum p.d.f.s in the lower-right and upper-left corner regions do not shrink, because these regions are in the 'separation bubbles' which are free from the sweeping effect. In the lower-right and upper-left corner regions there appear roughly steady buoyancy-driven secondary vortices, and thus the contribution of instantaneous vortices to the p.d.f. therein cannot be distinguished from that of the buoyancy-driven secondary vortices. More frequent appearance of counter-clockwise vortices near the lower-right and upper-left corners (cf. Fig. 14 (d, e)) is a direct consequence of the buoyancy-driven roughly steady counter-clockwise vortices.

Let us now discuss the dynamical behavior of instantaneous streamwise vortices in the near-region of the corner. Since the vortical structures are elongated in the streamwise direction, and the effect of viscosity on them is not expected to be crucial, we shall consider the simplest inviscid model consisting of a streamwise vortex filament of strength $\gamma$, its three image filaments, and a fixed streamwise filament of strength $\Gamma > 0$ (clockwise rotation in Fig. 15) and its image filaments. The vortex filament of $\gamma$ represents the streamwise vortex tube, and the image filaments are used to express the effects of two impermeable walls. The fixed filament is introduced to approximately take into account the swirling effects of the large-scale circulation. In the real situation at low Reynolds numbers $Re_b = 3000$ and 4400, the inner and outer length scales are not separated from each other, so that the distances from the streamwise vortex to the duct center and to the walls (or the corner), $\ell_c$ and $\ell_w$, are of the same order. The velocity scale of the streamwise vortex in the corner region could be estimated as $\gamma/\ell_w$, while the large-scale circulation might have the velocity of the order of $\Gamma/\ell_c$ near the corner. Therefore, the velocity ratio of the circulation to the vortex should be of the order of $\Gamma/\gamma$, and at the same time it could also be estimated as $u_g/u_\tau$. Figure 15 shows the cross-sectional vector field, for the inviscid vortex filament, induced

by the inviscid filaments representing the impermeable walls and the large-scale circulation. for $\Gamma/\gamma(\sim u_g/u_\tau) = \pm 3.3$ $(Ri = 0.052, Re_b = 4400)$ and $\Gamma/\gamma(\sim u_g/u_\tau) = \pm 11.7$ $(Ri = 1.02, Re_b = 4400)$. It can be seen in Fig. 15 (b) for $|\Gamma/\gamma| = \pm 3.3$ that the vector field for the counter-clockwise vortex of $\gamma < 0$ provides closed trajectories near the corner so that the vortex can stay there. The vector field for the clockwise vortex of $\gamma < 0$ in Fig. 15 (a), on the other hand, does not allow closed trajectories, so that the vorex of $\gamma > 0$ cannot stay near the corner. This is because in the former case the geometrical constraint in the corner region can compensate the sweeping effect of the large-scale circulation, or equivalently the cross-streamwise velocity induced by the image vortices can compensate the one induced by the circulation. For $|\Gamma/\gamma| = 11.7$ (Fig. 15 (c)), however, the sweeping effect is much stronger, and thus it is possible only for the counter-clockwise vortex very close to the corner to stay there.

### B. Low-velocity streaks

Next, we define the positions of low-velocity streaks near the wall as those of local minima of the wall shear on each wall. We plot the p.d.f.s of the positions of the low-velocity streaks in Fig. 16(a, b). It can be seen that the localization of the near-wall structures (streaks) by the sweeping effects of large-scale circulation affects the mean profile of the skin friction and the heat transfer rate on the top and bottom walls. The frequent appearance of low-velocity (Fig. 16(a, d)) and high- (or low-) temperature streaks associated with the streamwise vortices also leads to the lower skin friction and heat transfer in the left (or right) corner region on the bottom (or top) wall in Fig. 16(c, d, e, f) for $Re_b = 4400$. The high-velocity and low- (or high-) temperature fluid is pushed towards the bottom (or top) wall by the large-scale convection, enhancing the skin friction and heat transfer in the right corner region in Fig. 16 (c, d, e, f).

In order to investigate the temporal evolution of the low-velocity streaky structures, we consider the streamwise-minimal turbulent flow which can be achieved by reducing the streamwise computational domain $L_x$ to the lowest value for sustaining turbulence [15]. Since in the minimal flow, the streamwise wavelength of the corrugated streaks coincides with $L_x$, their streamwise average may be used to represent the spanwise position of the streaks. We perform the DNS at $Re_b = 4400$ and $Ri = 0.052$ for $L_x/h = 4/9\pi$ $(L_x^+ = 214)$ in

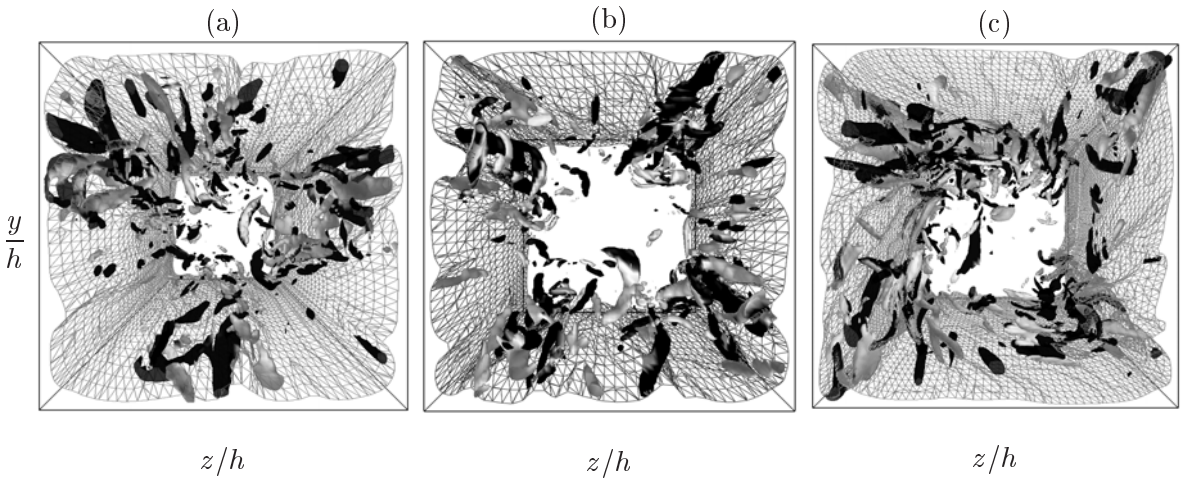


FIG. 13: The snapshots of instantaneous low structures at $Re_b = 4400$, (a) $Ri = 0.00026$ ($Gr = 5.0 \times 10^3$, in *regime* (I)), (b) $Ri = 0.052$ ($Gr = 1.0 \times 10^6$, in *regime* (II)), (c) $Ri = 1.03$ ($Gr = 2.0 \times 10^7$, in *regime* (III)). The streamwise velocity is shown by the gray iso-contour mesh at the level of 0.6 $u_b$, and the streamwise coherent vortices are shown by the iso-surfaces of the second invariant of velocity gradient tensor (Q-criterion) at the level of 0.03 $u_\tau^4/\nu^2$. The light objects are vortices with positive streamwise vorticity (the clockwise vortices) and the dark objects are vortices with negative vorticity (counter-clockwise vortices).

the *regime* (ii), where the buoyancy-driven velocity is comparable with the turbulence-driven mean secondary velocity. The minimum streamwise period to maintain turbulence in an isothermal square duct has been investigated systematically by Uhlmann *et. al.* [5], indicating that the minimum value is $L_x^+ \sim 190$, roughly independent of the Reynolds number.

In Fig. 17, we show the evolution of the low-velocity streaks by tracking the spanwise positions of local minima in the streamwise-averaged instantaneous wall shear profile. It can be seen onboth bottom and vertical walls that the low-velocity streaks are swept by the large-scale circulation towards the corner at $z/h = -1$ ($z^+ = -153.4$) in Fig. 17 (a) and at $y/h = 1$ ($y^+ = 153.4$) in Fig. 17 (b), and their spacing is roughly 100 wall units. In the near-region of the corner $y/h = 1$ on the vertical wall, however, another streak remains continuously located around $y/h = 0.5$ ($y^+ \approx 80$) and it is distinct from the usual low-velocity streaks. This stationary streak is located at the front of the 'separation bubble' (cf. Fig. 7 (g) and Fig. 9 (b)) and does not appear on the bottom wall. This result is another indication of difference between the buoyancy-driven mean secondary vortices and

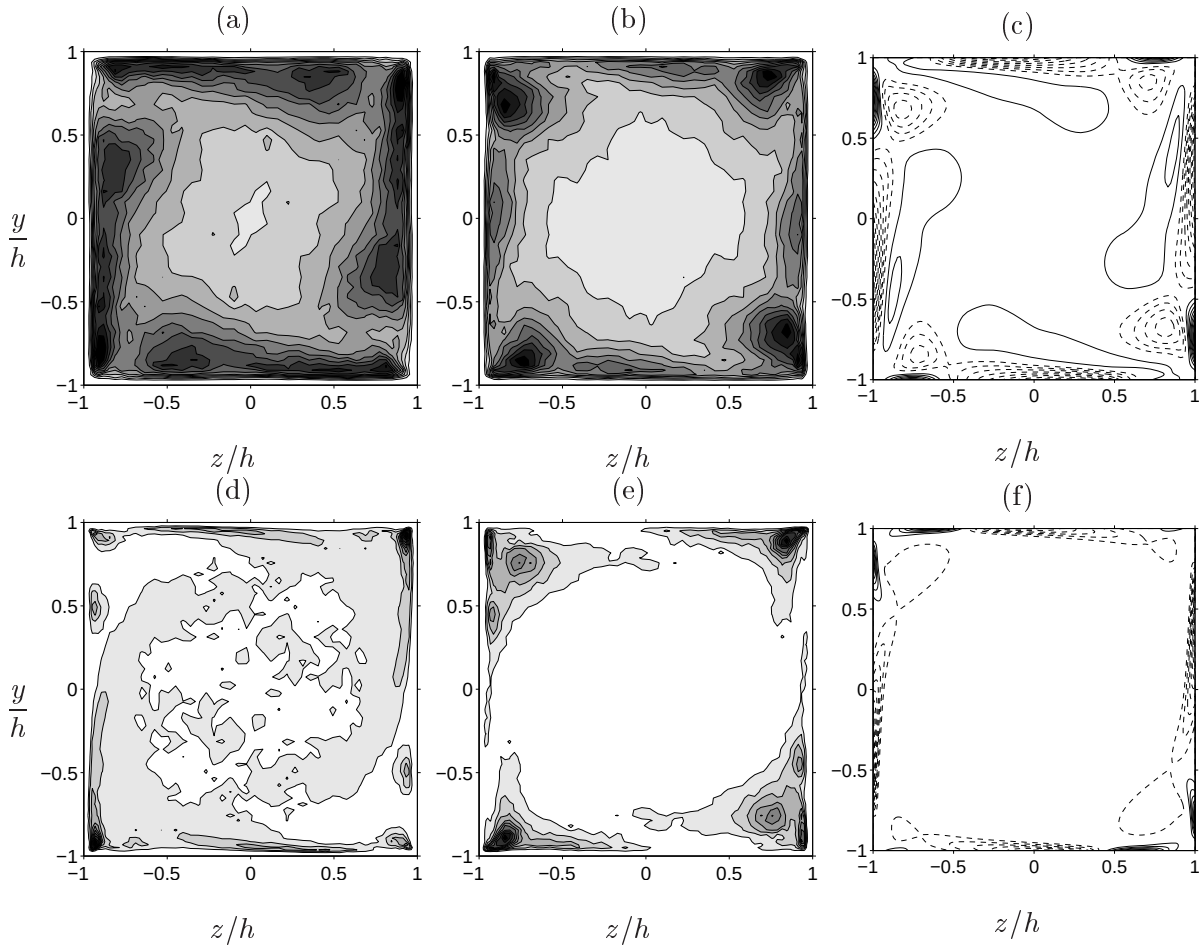


FIG. 14: P.d.f.s of the positions of the vortex centers and the mean streamwise vorticity, (a) with positive vorticity (i.e. clockwise vortices), (b) with negative vorticity (i.e. counter-clockwise vortices) at $Re_b = 4400$, $Ri = 0.052$ ($Gr = 1.0 \times 10^6$). The level of p.d.f.s is represented in gray scale (black is highest and white is lowest). (c) Mean streamwise vorticity, solid lines are positive (clockwise) and dashed lines are negative (counter-clockwise). (d-f) The same as (a-c), but for $Re_b = 4400$, $Ri = 1.03$ ($Gr = 2.0 \times 10^7$).

the turbulence-driven ones (the upper-left and lower-right vortices, and the upper-right and lower-left ones in Fig. 7 (c, g)).

## VII. CONCLUDING REMARKS

Direct numerical simulations of fully developed low-Reynolds-number turbulent flow in a horizontal square duct heated from below are performed at bulk Reynolds numbers $Re_b =$

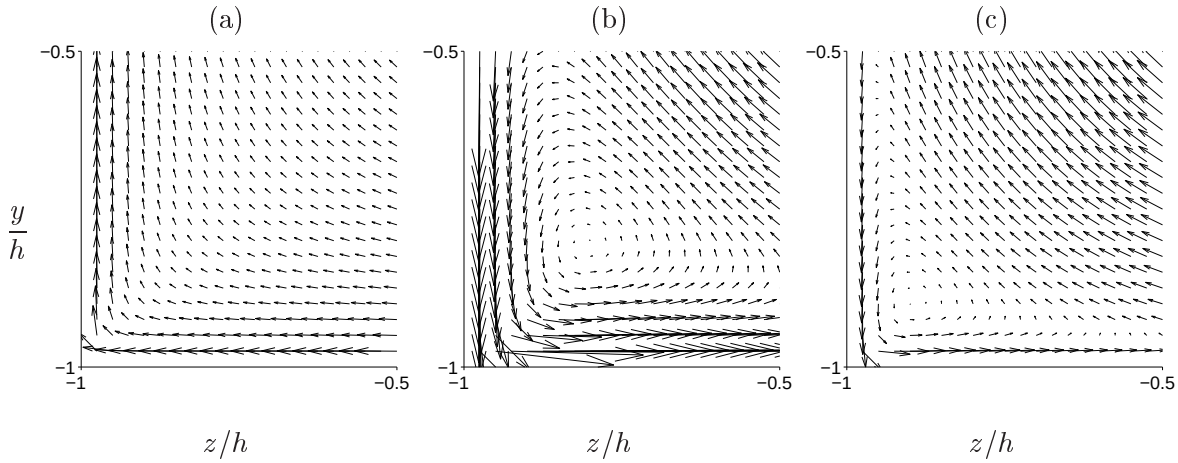


FIG. 15: Cross-sectional induced velocity vectors of vortex filaments under the effects of two impermeable walls and (clockwise) large-scale circulation represented by the filament of strength $\Gamma$ fixed at $(y/h, z/h) = (0, 0)$. (a) Vortex filament with positive (clockwise) strength $\gamma$ with $\Gamma/\gamma$ $(\sim u_g/u_\tau) = 3.3$. (b, c) Vortex filaments with negative (counter-clockwise) strength $\gamma < 0$ (b) with $\Gamma/\gamma$ $(\sim u_g/u_\tau) = -3.3$, (c) with $\Gamma/\gamma$ $(\sim u_g/u_\tau) = -11.7$.

$3000, 4400$ and bulk Richardson numbers $0 \leq Ri \leq 1.03$ in order to demonstrate the effects of buoyancy on turbulence statistics and structures, with emphasis on characterization of the mean secondary flows of Prandtl's first and second kinds in terms of coherent vortical structures, thermal convection, and their interaction.

At small Richardson numbers $0 \leq Ri \lesssim 0.025$ no visible change is observed in global properties of turbulent flow, such as mean friction factor, mean Nusselt number and secondary-flow velocity. For this range of $Ri$ the mean secondary flow is characterized by four pairs of turbulence-driven counter-rotating vortices similar to those in an isothermal duct.

For $Ri \gtrsim 0.025$ the cross-stream thermal convection represented by single large-scale circulation is found to appear to affect the turbulence field. The sense of the circulation depends on an initial condition, and once forming its sense does not alternate. It is observed that the four mean secondary-flow vortices of the same sense of the circulation disappear while those of the opposite sense remain near the corners. The near-wall coherent structures are observed in the corner region more frequently than around the wall bisector, since they are swept along the wall by the large-scale convection toward the corner. These structures contribute the shift of the intense region of the streamwise r.m.s velocity and r.m.s. temperature towards the corners. The four small-scale mean secondary flow vortices appear as a

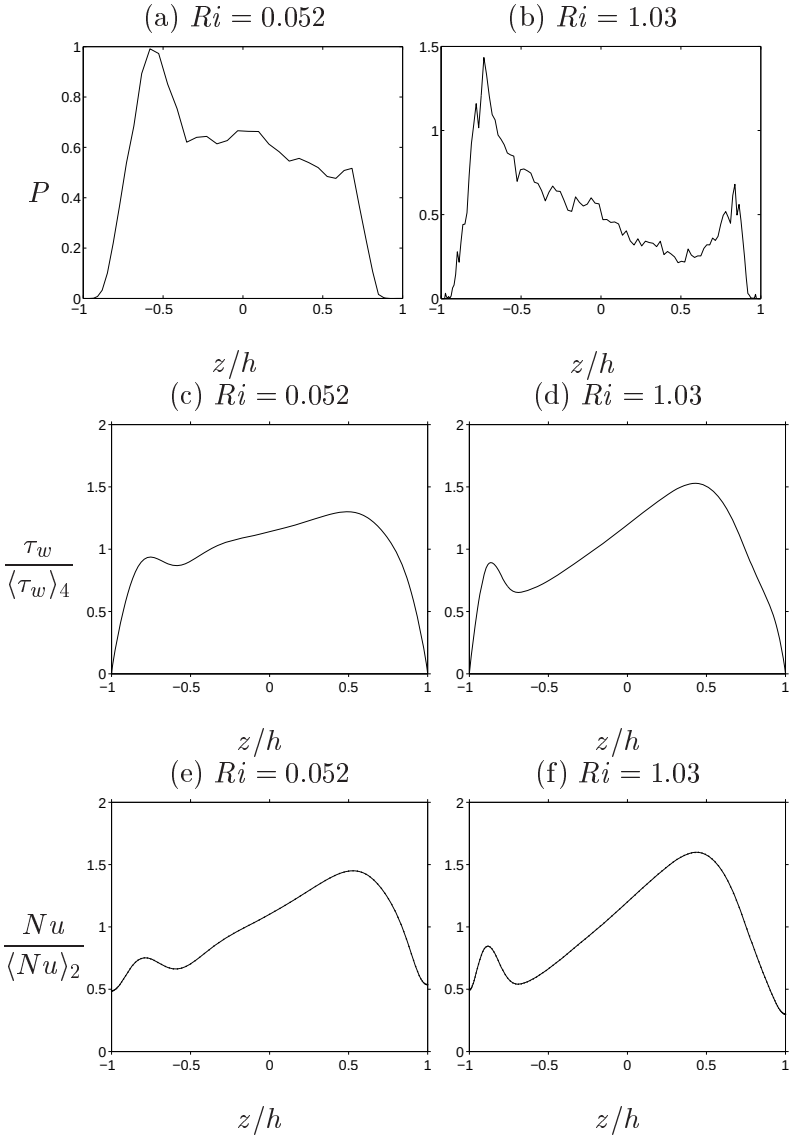


FIG. 16: P.d.f.s of the positions of low-velocity streaks, $P$ (a, b), wall shear stress (c, d), and Nusselt number (e, f) on the bottom wall $y/h = -1$ at $Re_b = 4400$. (a), (c), (e) $Ri = 0.052$, (b), (d), (f) $Ri = 1.03$.

statistical footprint of the near-wall coherent structures (streamwise vortices), which is the same generation mechanism as in the case of the mean secondary flow of Prandtl's second kind in the iso-thermal low-$Re$ turbulent flows.

It is found that for $Ri \gtrsim 0.025$ the mean friction factor, the mean Nusselt number, the secondary-flow velocity, and r.m.s. velocities and temperature increase with increasing $Ri$ under the action of buoyancy.

At $Ri \gtrsim 0.25$

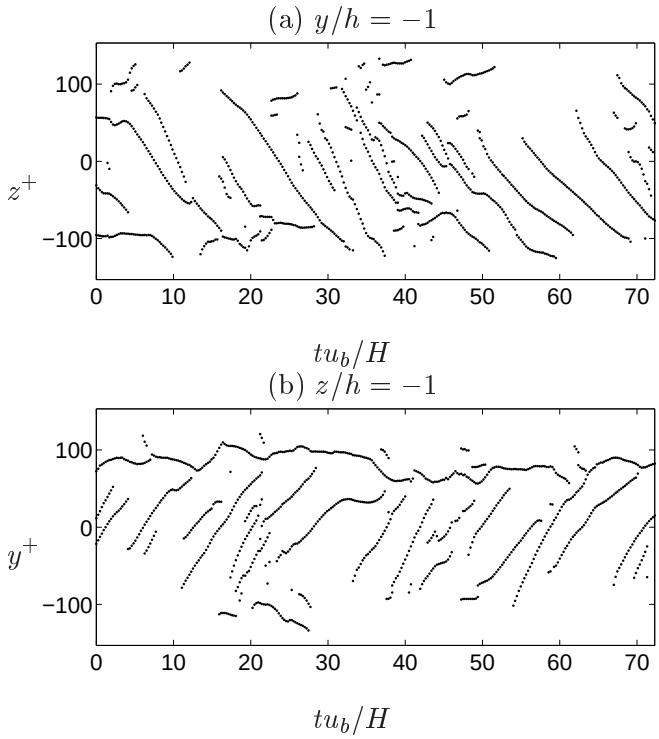


FIG. 17: Temporal evolution of the position of low-velocity streaks in the streamwise minimal turbulent flow at $Re_b = 4400$, $L_x/h = 4/9\pi$, $L_x^+ = 214.2$, $Ri = 0.052$; (a) on the bottom wall $y/h = -1$ and (b) on the vertical wall $z/h = -1$.

At $Ri = 1.03$, eventually just two mean counter-clockwise vortices near the upper-left and lower-right corners remain significant since these mean vortices are associated with the large-scale circulation induced by the buoyancy force. The two small-scale vortices near the upper-right and lower-left corners of the mean secondary flow still appear as a statistical footprint of the near-wall coherent structures (streamwise vortices).

The characteristics of the small-scale vortices near the corners have been confirmed quantitatively by scaling of the corresponding position of the local minima of the mean streamwise vorticity. The positions of the local minimum of the streamwise vorticity of the secondary flow vortices related to the near-wall coherent structures scale in wall units [12]. It is obvious that the buoyancy-driven small-scale secondary flow vortices (near the lower-right and upper-left corners in Fig. 7(d, h) and Fig. 9) have the size of outer scale.

The corner behaviour of a vortex filament with the large-scale circulation using a simple kinetic model can explain the probability of the appearance of quasi-streamwise vortices. The counter-clockwise vortex filaments should be located close to the corner to stay longer

in the corner region against the advection induced by the clockwise circulation, which leads to the shrink of the lower-left and upper-right secondary flow vortices.

The localization of the near-wall coherent structures (quasi-streamwise vortices and low- and high-speed streaks) in the corner regions also affects skin friction and heat transfer rate on the wall near the corners.

The effects of near-wall coherent structures play significant roles in the generation of the secondary flow and cross-sectional distribution of the turbulent statistics in such anisotropic flow like a square duct. More details of buoyancy effects on the behaviour of turbulent structures at higher Reynolds numbers, i.e. not only the near-wall small-scale structures but large-scale structures, should be revealed quantitatively in order to improve turbulent models or to predict turbulence effects precisely.

**Acknowledgements**

A. S. is supported by JSPS Research Fellowship for Young Scientists. G. K. is partially supported by Grant-in-Aid for Scientific Research (B) from JSPS. The present computations were performed with the use of computing system for research at Kyushu University and supercomputing resources at Information Technology Center at the University of Tokyo. The authors would like to thank Professor Sadayoshi Toh for his inquiry for the formation mechanism of the flow pattern of two-dimensional thermal convection in a square container heated from below.

---

[1] P. Bradshaw. Turbulent secondary flows. *Ann. Rev. Fluid Mech.*, 19:53-74, 1987.

[2] C.M. Winkler, Sarma L. Rani and S.P. Vanka. Preferential concentration of particles in a fully developed turbulent square duct flow. *Int. J. Multiphase Flow.* 30:27-50, 2004.

[3] F. B. Gessner The origin of secondary flow in turbulent flow along a corner. *J. Fluid Mech.*, 58:1-25, 1973.

[4] S. Gavrilakis. Numerical simulation of low-Reynolds number turbulent flow through a straight square duct. *J. Fluid Mech.* 244:101-129, 1992.

[5] M. Uhlmann, A. Pinelli, G. Kawahara and A. Sekimoto. Marginally turbulent flow in a square duct. *J. Fluid Mech.* 588:153-162, 2007.

[6] M. Salinas Vázquez and O. Métais. Large-eddy simulation of the turbulent flow trough a heated square duct. *J. Fluid Mech.* 453:201-238, 2002.

[7] L.-D. Ma, Z.-Y. Li and W.-Q. Tao. Direct numerical simulation of turbulent flow and heat transfer in a square duct with natural convection. *Heat Mass Transfer* 44:229-250, 2007.

[8] J. Mizushima and T. Adachi. Sequential transition of the thermal convection in a square cavity. *J. Phys. Soc, Japan* 66(1):79-90, 1997.

[9] R. Verzicco and P. Orlandi. A finite-different scheme for three-dimensional incompressible flows in cylindrical coordinates. *J. Comput. Phys.* 123:402-414, 1996.

[10] P. Haldenwang, G. Labrosse, S. Abboudi and M. Deville. Chebyshev 3-d spectral and 2-d pseudo-spectral solvers for Helmholtz equation. *J. Comput. Phys.* 55:115-128, 1984.

[11] G. Kawahara, K. Ayukawa, J. Ochi, F. Ono and E. Kamada. Wall shear stress and Reynolds stresses in a low Reynolds number turbulent square duct flow *Trans. JSME B.* 66(641):95-102, 2000, (*in Japanese*).

[12] A. Pinelli, M. Uhlmann, A. Sekimoto and G. Kawahara. Reynolds number dependence of mean flow structure in square duct turbulence. *J. Fluid Mech.*, 644:107-122, 2010.

[13] A. A. Wray and J. C. R. Hunt. Algorithms for classification of turbulent structures. *In Topological Fluid Mechanics* (ed. H. K. Mofatt and A. Tsinober, Cambridge University Press), 95-104, 1990.

[14] S. Kida and H. Miura. Swirl condition in low-pressure vortices. *J. Phys. Soc. Japan* 67(7):2166-2169, 1998.

[15] S. Toh and T. Itano. Interaction between a large-scale structure and near-wall structures in channel flow. *J. Fluid Mech.* 524: 249-262, 2005.